Fabrication of Layered Double Hydroxide Microcapsules Mediated by Cerium Doping Metal-Organic Framework for Boosting Water Splitting

Huajie Xu [a,b], Changfu Shan [a], Xiaoxia Wu [a], Mingzi Sun [c], Bolong Huang*[,c], Yu Tang*[,a], and Chun-Hua Yan*[,a]

Micro-/nanocapsules assembly holds great potential for catalysis, storage, and drug delivery due to their modifiable shell, high exposed surface, and large accommodation space. Here, an ingenious one-step reaction strategy is presented to fabricate layered double hydroxides (LDHs) microcapsules, which benefit from the oxyphilic and synergistic coordination of Ce species to stabilize the initial morphology of metal-organic framework (MOF). Taking advantage of this unique superstructure, the as-prepared Ni-Fe-Ce-LDH microcapsules demonstrate an excellent oxygen evolution reaction (OER) activity with an overpotential of 242 mV at 10 mA cm^{-2} and at least long-term durability of 24 h. Density functional theory (DFT) results further confirm the electronic modulation induced by the Ce doping for both subtle 3D LDHs architectures and superior OER performances. This work not only provides insight into the rare-earth (RE) doping mediated crystal growth and transformation process of MOFs but also represents a facile way to fabricate the desired microcapsule superstructure in virtue of the Lewis acid property and synergistic coordination of RE-ions.

Introduction

Micro- and nanocapsules have become the research interest in the various promising fields including catalysis, storage, and drug delivery on account of their modifiable shell, high exposed surface, and large accommodation space.[1-4] Currently, capsules are commonly fabricated in the presence of soft or solid templates in virtue of various microencapsulation techniques, such as coacervation, lyophilization, fluidization, extrusion, and spray-drying.[5-8] Using such self-assembled architectures, micro-/nanocapsules with the uniform size can be achieved, however, these approaches typically involve multi-step processes, requiring complicated synthesis or fabrication procedures. Moreover, based on these post-loading strategies suffers from the presence of the synthetic template, which significantly restricts their function and practical applications of the resulting micro-/nanocapsules. [7, 9] Thus, in order to extend the applicability of capsular nanocrystals, the development of effective and facile fabrication and encapsulation strategies are highly needed.

Layered double hydroxides (LDHs) are important two-dimensional (2D) layered materials with the edge-sharing $M(OH)_6$ octahedra forming ultrathin nanosheets layers and the metal cations are uniformly distributed at the atomic level. For the past few years, the LDHs and their nanocomposites have been widely applied in adsorption materials, pharmaceutics, functional material precursors, and heterogeneous catalysis.[10,11] Particularly, the NiFe-LDH based electrocatalysts have evolved into a major interdisciplinary research focus due to its superior catalytic activity for oxygen evolution reactions (OER) and regarded as the most promising alternatives for precious metal catalysts.[12-15] Constructing hierarchical three-dimensional (3D) architectures based on 2D LDHs can effectively suppress the aggregation of LDH nanosheets with a higher surface-exposed active site density and, therefore, is an effective strategy for creating more edge active sites to boost the OER activity of Ni-Fe-LDH-based electrocatalysts.[16-18] Very recently, great efforts have been made to designed 3D configuration (oxy)hydroxides towards water splitting with encouraging results such as nanospheres, nanosheets, nanoprisms, nanoboxes, nanocages, polyhedrons, and nanotubes, thus the acquired composites exhibited high OER electrocatalytic activity.[19-22] Notwithstanding these advances, most of the catalysts usually are fabricated by complicated multi-step synthesis strategies to obtain 3D hollow nanostructure catalysts, which largely limit its further development for practical applications.

Rare-earth (RE) elements have made great progress in phosphors, catalysts, and magnets, owing to the unique properties of 4f-electrons.[23-25] Recent researches show that RE ions can provide additional tunability for metal-organic frameworks (MOFs) including fascinating topologies,[26,27] enhanced photoresponses,[28,29] excellent temperature indicators,[30-31] and controllable pore environments.[32,33] More importantly, the introduction of RE ions may stabilize the reactive intermediates.[34-38] Cerium, as one of the most abundant RE elements, is particularly attractive for its rich redox properties, good electronic/ionic conductivity, and flexible coordination ability.[39-41] The multi-valence property of Ce ions will offer a flexible opportunity to generate strong electron interactions with other metal cations and ligands.[42-44] Meanwhile, cerium ion possesses high, flexible coordination number and oxyphilic coordination ability, which is considered as a hard Lewis acid with easy bonding formation with hard oxygen ligands, effectively participating as buffer guards to prevent the attack from alkaline media, and slowing down the metal-ligand bond dissociation process.

The main target of this study is to simply fabricate a 3D LDHs microcapsules superstructure. Herein, we demonstrate an improved competitive coordination strategy by virtue of the Ce ions doping to synthesize uniform and hollow 3D LDHs microcapsules through a facile one-step solvothermal reaction (Fig. 1). In the early stages of the reaction, the formed MIL-88A becomes more stable under the coordination of Ce^{3+} ions doping, especially in weak alkaline solutions. As the reaction progresses, the urea releases more hydroxide, which prompts the dissolution of the inner core and the precipitation of Fe^{3+}, Ni^{2+}, and Ce^{3+} ions to construct a hierarchical shell with vertically and interconnected Ni-Fe-Ce-LDH nanosheets on the outer layer of the MOF precursors. Under precise control of Ce^{3+} ions concentration, the well-defined hierarchical Ni-Fe-Ce-LDH hollow microcapsules are finally obtained. Our as-prepared Ni-Fe-Ce-LDH microcapsules loaded on glassy-carbon electrodes

demonstrate a low overpotential of 242 mV at 10 mA cm^{-2} and a highly stable current density at least 24 h in alkaline conditions for OER. The well-defined competitive coordination architecture of LDHs microcapsules allows us to explore an effective synthetic strategy towards creating more functional microcapsules. Furthermore, the reaction mechanism and active sites of the Ni-Fe-Ce-LDH microcapsules are proposed by a combination of experiments and DFT calculations. This work supplies valuable references to guide the future developments on the fabrication of the unique superstructure electrocatalysts mediated by the facile and applicable cerium doping MOFs strategy.

Results and Discussion

Construction and analysis of 3D LDHs microcapsules

The fabrication process of Ni-Fe-Ce-LDH microcapsules is schematically shown in Fig. 1. The Ni-Fe-Ce-LDH microcapsules were synthesized via a one-step hydrothermal approach using a detailed description of the experimental methods given in the Supporting Information. In brief, fumaric acid, urea, and metal salts ($Fe(NO_3)_3{\cdot}9H_2O$, $Ni(NO_3)_2{\cdot}6H_2O$, $Ce(NO_3)_3{\cdot}6H_2O$) were dispersed in aqueous solution. Ni-Fe-Ce-LDH microcapsules with different morphologies were prepared by adjusting Ce^{3+}/Fe^{3+} ion ratios via the hydrothermal process, and the total concentration of metal ions remained constant throughout the process. The structural information of the synthetic Ni-Fe-Ce-LDH microcapsules was obtained by X-ray diffraction (XRD) analysis (Fig. S1). The peaks at 11.8°, 23.1°, 34.6°, and 60.3°can be assigned to (003), (006), (012), and (110) facets of the hydrotalcite-like structure.[45,46] Meanwhile, XRD analysis indicated that when the doping concentration of Ce^{3+} ions less than 40%, the LDHs phase can crystallize well in these composites. In addition, the diffraction peaks gradually widen with the increase of Ce doping ratio, which might be due to the formation of smaller size LDHs with lattice distortion inducing from a much larger ionic radius of Ce^{3+} (102 pm) than Fe^{3+} (55 pm).[41,47]

The scanning electron microscopy (SEM) images (Fig. 2a) clearly revealed that the as-formed 30%Ce-Ni-Fe-LDH microcapsules exhibited uniform 3D hierarchical nanocrystalline morphology with an average length of about 1 μm. An enlarged SEM image showed that the 2D Ce-Ni-Fe-LDH nanosheets were predominantly oriented vertically on the surface of the microcapsule nanocomposites to form a hierarchical shell (Fig. 2b). Transmission electron microscopy (TEM) and high angle annular dark-field scanning transmission electron microscopy (HAADF-STEM) images (Fig. 2c,d) showed that the uniform microcapsules possessed hollow cavity with a diameter of approximately 250 nm, and the internal cavity of the LDHs microcapsules can be clearly shown by the strong contrast between the lamellar shell and the legible central void space.

A magnified TEM image showed folded edges or wrinkled layers, indicating ultrathin nature for LDHs nanosheets (Fig. 2e). Furthermore, loosely stacking of the interconnected LDHs nanosheets form a highly porous structure, so the Ni-Fe-Ce-LDH microcapsules exhibit a high Brunauer-Emmett-Teller (BET) specific surface area of 286.33 m^2/g (Fig. S2). Moreover, the lattice fringe with a spacing of 0.26 nm should be attributed to the (012) plane of LDHs, which further confirmed the formation of LDHs structure, meanwhile selected area electron diffraction pattern in the inset explained the hexagonal phase of Ni-Fe-Ce-LDH (Fig. 2f).

To investigate the spatial elemental distribution, energy-dispersive X-ray spectroscopy (EDX) mapping analysis was employed on an individual 30%Ce-NiFe-LDH hollow microcapsule. The results clearly demonstrated the uniform distribution of Ni, Fe, and Ce ions throughout the hollow nanoframe (Fig. 2g). A magnified mapping analysis further confirmed that Ni, Fe, and Ce ions were evenly distributed on the interconnected LDHs nanosheets (Fig. 2h). The corresponding EDX spectrum also confirmed the existence of Fe, Ce and Ni elements (Fig. S3). The relative contents of elements were also determined by inductively coupled plasma atomic emission spectroscopy (ICP-AES) (Table S1).

In order to reveal the important role of Ce species in regulating the growth of Ni-Fe-Ce-LDH microcapsules by the one-step solvothermal process, adjusting the doping ratio of Ce ions for the morphology of the as-obtained samples was monitored through TEM and SEM. When Ce^{3+} ions are absent in the reaction system, the 3D capsule-shaped LDHs cannot be obtained (Fig. 3a). With the increase of Ce^{3+} doping amount from 5% to 50%, uniform Ni-Fe-Ce-LDH microcapsules gradually formed and the average length of these Ni-Fe-Ce-LDH microcapsules decreased from 2 to 1 μm, and the average width grew from 200 to 300 nm (Fig. 3b-f). Remarkably, these microcapsules maintain a good LDHs crystalline phase (Fig. 3g). However, when Ce^{3+} doping content exceeded 30%, a large number of nanoparticles were generated on the capsule shell (Fig. S4), which is attributed to the formation of metal oxide nanoparticles. This point was vrified by the O 1s XPS spectra of 5%Ce-Ni-Fe-LDH and 50%Ce-Ni-Fe-LDH as shown in Fig. S5. The O1 peak at ~529.6 eV was assigned to the metal-O band.[48-50] The area of O1 in 50% Ce-Ni-Fe-LDH increased dramatically, which confirmed that a large amount of metal oxide was formed when the concentration of Ce^{3+} doping reached 50%. Meanwhile, Ce^{3+} doping content also had a similar effect on the structure and morphology of MIL-88A (Fig. S6a-d), and their aspect ratios become smaller as Ce^{3+} increases. However, XRD patterns showed that the doping process did not bring too much change in the crystal structure (Fig. S7).

It was worth noting that the urea dose played a crucial role in controlling the formation of the hollow cavity and the growth of the Ni-Fe-Ce-LDH microcapsules during the hydrolysis reactions (Fig. S8a-e). Appropriately increasing the amount of urea in the reaction system accelerated the transformation. In the initial reaction period, a small amount of urea hydrolyzed and assisted Ce^{3+} in coordination with fumaric acid to stabilize the MIL-88A, and then a large amount of urea hydrolysis produced a strong alkali environment, which further

promoted the conversion of MIL-88A into hollow capsule-shaped structures. Therefore, the accurate control of urea content was also an important factor to achieve competitive coordination to obtain capsule-shaped LDHs nanosheets structure around the MOFs template surface. However, too much urea also induced the formation of larger LDHs nanosheets with the formation of bulk products (Fig. S8f and Fig. S9), which was ascribed to the direct precipitation of some metal ions in a strongly alkaline solution.

Role of Ce

The important role of Ce-doping in the successful one-step synthesis of Ni-Fe-Ce-LDH microcapsules was investigated. For nanocrystalline materials MIL-88A, Ce ions doping may play a key role in stabilizing a specific crystalline phase and modifying electronic properties. Moreover, it is worth noting that Ce ions possess excellent properties of multivalence, flexible coordination, and high affinity for hard oxygen donors. Based on these properties, the introduction of Ce ions can effectively regulate the growth process to optimize the crystallographic stability, morphology, and properties of the resulting nanocrystals.

The X-ray photoelectron spectroscopies (XPS) were firstly carried out to investigate the electronic structures of the samples. XPS results in Fig. 3h showed that the main Fe 2p peaks of the Ni-Fe-LDH located at 710.5 and 724.2 eV, which suggested that Fe mainly existed in the +3 state in the Ni-Fe-LDH. In comparison, the binding energies of Fe 2p in the Ce ion doped Ni-Fe-Ce-LDH shifted to higher energy by 0.4-1.5 eV relative to that of the Ni-Fe-LDH, which indicated a strong electronic interaction between Ce and Fe ions responsible for high-valence $Fe^{\delta+}$ ($3 < \delta < 4$) species dominating in the Ni-Fe-Ce-LDH. These interior high-valent Fe ions could be much more active kinetically and promote the water oxidation process.[51-53]

The XPS results also showed that there was no significant difference for the nickel element in both the Ni-Fe-LDH and Ni-Fe-Ce-LDH (Fig. 3i). Therefore, these results suggested that the atomic and electronic configurations of Fe sites within the Ni-Fe-Ce-LDH were redistributed with the crystal structure evolution by doping the Ce ions into the hierarchical laminate, and Ni only served as the electron transfer bridge for promoting the charge transfer between Ce and Fe ions. Meanwhile, the high-resolution Ce 3d spectrum showed the multiplet splitting of Ce^{3+} and Ce^{4+} indicating that Ce^{3+} and Ce^{4+} coexisted in this hybrid system (Fig. S10), and the $Ce^{3+}\leftrightarrow Ce^{4+}$ redox transformation can induce the generation of oxygen vacancies, thus ensuring good electron transport. In addition, the higher electron affinity of Ce^{4+} was attributed to the main reason for modulating the electronic structure and catalytic active sites. Therefore, it is an effective approach to achieve excellent electrocatalytic performances by introducing suitable cations to tune the crystal and electronic structures of transition metal based materials.

To further examine whether high-valent state RE elements played an important role in the one-step synthesis of RE-doping LDHs, we also performed the experiments with doping of other RE elements including La, Pr, Eu, Tb, Dy and Lu (Fig. S11 and Fig. S12). However, only Tb was found to be able to induce one-step synthesis of homogeneous 3D Ni-Fe-Tb-LDH microcapsules in a similar way to Ce. The SEM and TEM images (Fig. S13a,b) revealed that the Ni-Fe-Tb-LDH possessed a hierarchical shell with vertically and interconnected 2D LDHs nanosheets. XRD pattern (Fig. S14) confirmed the formation of the LDHs phase with the introduction of Tb^{3+}. The EDX spectra signals for the Tb element were also clearly observed besides signals for Ni and Fe, further confirming the successful introduction of Tb ions into the hierarchical microcapsules (Fig. S15). The EDX mapping analysis of Ni-Fe-Tb-LDH (Fig. S16) also can clearly demonstrate the uniform distribution of Ni, Fe, and Tb throughout the hollow nanoframe. Ce is the unique case that it achieves +4 valence state easily and flexibly switches between +3 and +4 valence state, which is the key for creating oxygen vacancies and guaranteeing good electron transport. Compared to other RE ions, Tb is the most possible element to realize similar high valence state switching between +3 and +4 (Tb^{4+}/Tb^{3+}= +3.1 V vs. NHE), which leads to the formation of the hollow microcapsules.[54,55] Previous work has investigated the electronic structures of the lanthanide oxide systematically, in which CeO_2 and Tb_2O_3 show the similar 4f occupied levels.[56]

Electrochemical performances

The electrochemical OER activities of various Ni-Fe-Ce-LDH in 1 M KOH aqueous solution were examined using a standard three-electrode system. We first compared the catalytic performances of Ni-Fe-Ce-LDH and Ni-Fe-LDH microcapsules which were derived from the MIL-88A template (see the Supporting Information for experimental details). Fig. 4a compares the iR-corrected cyclic voltammetry (CV) curves of 30% Ce-Ni-Fe-LDH and Ni-Fe-LDH. Compared with the Ni-Fe-LDH sample, the 30% Ce-Ni-Fe-LDH showed an earlier redox peak and only requiring a 242 mV overpotential for 10 mA cm^{-2} (Fig. 4a), which was 49 mV lower than NiFe-LDH. Such outstanding electrocatalytic properties can be attributed to synergic effects derived from Ce-doped NiFe-LDH resulting in stronger adsorption to *OH. Inherent properties of OER anodes also were evaluated by the Tafel slope originating from the LSV curves (Fig. 4b). The 30%Ce-Ni-Fe-LDH catalyst possessed an extremely small Tafel slope of 34 mV dec^{-1}, which was much lower than 61 mV dec^{-1} of Ni-Fe-LDH and 59 mV dec^{-1} of Ir/C, reflecting superb OER kinetics of Ni-Fe-Ce-LDH during OER process, even comparable to the performance of the most reported MOF-derived and LDHs-based electrocatalysts (Table S2 and Table S3).

The introduction of Ce species effectively induced a one-step formation of LDHs microcapsules, and the effect of Ce-doped amount on catalytic performance was also investigated in detail. As shown in Fig. 4c, when the Ce doping ratio is less than 40%, the obtained catalysts exhibited lower overpotential and higher current densities relative to Ni-Fe-LDH. The 30%Ce-NiFe-LDH

exhibited the lowest overpotential of 242 mV for the OER process at 10 mA cm^{-2}, which was smaller than NiFe-LDH (291 mV), 5.0%Ce-NiFe-LDH (281 mV), 10%Ce-NiFe-LDH (274 mV), 20%Ce-NiFe-LDH (264 mV), and 40%Ce-NiFe-LDH (251 mV). Notably, the reported Ce doped catalysts have shown much higher performances than the state-of-art OER catalyst RuO_2 (Fig. 4c). Additionally, 30% Ce-NiFe-LDH has the largest turnover frequency (TOF) of 0.011 S^{-1} at an overpotential of 300 mV, revealing higher intrinsic catalytic activity for 30%Ce-NiFe-LDH toward OER (Table S4). In Fig. 4d, the Tafel slope and the overpotential of Ni-Fe-Ce-LDH were plotted with the doping ratio of Ce^{3+}, both of which decreased when the doping ratio was less than 40%, and the results indicated that the Ce doping ratio was positively correlated with improvement of OER reactivity.

In addition to changing the adsorption energy of oxygen-containing intermediates, the introduction of Ce ions may also affect the number of catalytic active sites. Therefore, the electrochemically active surface area (ECSA) has also been determined by investigating the CV measurement (Fig. 4e and Fig. S17). 30%Ce-Ni-Fe-LDH exhibited more effective ECSA and the greater exposure of the catalytically active surface area. To probe the charge transfer processes, electrochemical impedance spectroscopy (EIS) also were measured (Fig. S18). The smaller semicircle of Nyquist plots for 30%Ce-NiFe-LDH indicated lower charge transfer resistance (R_{ct}) promoting faster charge transport and thus improved reaction kinetics in favor of obtaining more superior catalytic activity.

The long-term durability is an important challenge since the unsupported 3D framework is prone to degenerate from long-term exposure to electrolytes. The operational stability of 30%Ce-NiFe-LDH was investigated by long-term chronopotentiometry and CV scanning 500 cycles (Fig. 4f). The OER catalytic activity of 30%Ce-NiFe-LDH can maintain for at least 24 h, and the CV curve also shows negligible change after 500 cycles, and the XRD pattern after OER shows almost no obvious structural changes (Fig. S19). Moreover, the SEM image clearly shows that the morphology can be retained completely after the long-term electrolysis (Fig. S20). The above experimental results indicate that the Ni-Fe-Ce-LDH microcapsules materials have excellent electrocatalytic activity and stability for OER.

DFT Elucidation of the doping Ce

In the end, we apply the DFT calculations to investigate the doping of Ce and OER performances. The pristine MIL-88A structure demonstrated that the electroactive region mainly located at the middle core part of MIL-88A, connecting by the C-C bonds (Fig. S21a). Regarding the projected partial density of states (PDOSs), we noticed that Fe-3d, O-2p, and C-2p orbitals form strong p-d couplings, which leads to a stable lattice structure. The electronic distribution near the Fermi level (EF) mainly located at Fe sites (Fig. S21b). Consistent with the experiments, we have investigated different doping positions and doping concentrations of Ce ions in MIL-88A. For the Ce doping at the Fe sites with low concentration, the electronic distributions were not evidentially affected (Fig. 5a). As the Ce doping concentration doubles, we noticed the electroactive region on the nearby C-O bonding (Fig. 5b). In comparison, the Ce doping in the pore position in MIL-88A was also highly possible, in which the electronic distributions were evidentially disturbed (Fig. 5c). Meanwhile, for the formed Ni-Fe-Ce-LDH, the electroactive region mainly locates near the Fe and Ni sites, further supporting the high electron transfer pathway to guarantee the OER performance (Fig. 5d). For the electronic structures with the Fe substitution by Ce at different concentrations, the PDOS of Ce-4f orbitals indicates that the valence of dopant Ce is closer to the Ce^{4+} as in CeO_2. Moreover, the introduction of Ce ions will not influence the electroactivity of the neighboring Fe sites. Fe-3d orbitals still locate close to the Fermi level (E_F), confirming the potential of high valence as experiments (Fig. 5e-f). Notably, for the Ce stabilization in the pores, Ce-4f orbitals become more similar to pure metal Ce, indicating the initial stabilization region for Ce during LDHs synthesis. Notably, the zero-valence Ce dopant significantly disturbs the electronic activity of nearly Fe sites, where the 3d-orbitals of Fe sites shift towards the higher valence states. These findings are consistent with the strong electronic interaction between Ce and Fe ions by XPS results (Fig. 5g). The PDOS of formed Ni-Fe-Ce-LDH further explains the origins of the superior OER performance. Ni-3d and Fe-3d orbitals both contribute to the high electroactivity, in which Ni-bands occupies the E_V-1.25 eV (E_v = 0 eV) while Fe-3d orbitals cross the E_F, supporting the stabilization of O-related species. The Ni-3d band has been pinned by the Fe and Ce positions at the appropriate position to preserve the high electroactivity during OER. Meanwhile, the Ce-4f orbitals show the overlapping with both Ni-3d and Fe-3d orbitals, which play as the electronic modulator to enhance the electron transfer throughout the catalyst surface (Fig. 5h).

From the energetic perspective, doping in the pore position within MIL-88A is more energetically favorable than directly doping at Fe sites. As Ce dopant concentration increased, the energy barrier for doping Fe sites also increased (Fig. 5i). These results illustrate that Ce dopants are highly possible to occupy the pore structure of MIA-88A, which modifies the electronic structure of the nearby Fe sites. After the introduction of Ce in the lattice, the Fe-O bond length has not been evidentially changed, which demonstrates the good stability of the MOF structure (Fig. 5j). For the OER process, under U = 0 V (standard potential), the Ni-Fe-Ce-LDH system shows the potential determining step (PDS) at the formation of [*OOH+H_2O+OH] from [O*+H_2O+2OH] with an energy barrier of 1.51 eV (Fig. 5k). After 1.23 V potential has been applied to the system, the overpotential for OER has been calculated to be 0.28 eV, which is in good agreement with the electrochemical testing result (Fig. 5l). Therefore, the Ce dopant is playing an essentially important role in both the structural

transformation and the efficient OER process, which is attributed to the strengthened electron transfer by the Ce-4f band modulation with *d-f* couplings.

Conclusions

In summary, we have demonstrated a facile one-step synthesis strategy to construct the delicate 3D LDHs microcapsules through utilizing the competitive coordination and high affinity for oxygen of cerium species to stabilize the initial morphology of MIL-88A. By rationally regulating the amount of doping Ce ions and urea, the aspect ratios of Ni-Fe-Ce-LDH microcapsules superstructure can be easily controlled. The unique 3D Ni-Fe-Ce-LDH microcapsules demonstrated the superior OER performance with a low overpotential of 242 mV at 10 mA cm^{-2} as well as long-term durability for at least 24 h. Through the DFT calculations, the significant role of Ce ions dopants is revealed on the optimization of the local electronic structures for OER and the facilitation to the morphological transformation mechanism during synthesis. These findings not only provide valuable insightful knowledge for the understanding of RE-doping in the crystal growth process regulation but also supply a general strategy based on the Lewis acid properties and oxyphilic coordination ability of RE ions for the future structure design and fabrication of microcapsule structures. Therefore, this work further broadens the RE-mediation strategy applications in the future design of novel catalysts and materials fabrication.

Conflicts of interest

There are no conflicts to declare.

Acknowledgements

This work was financially supported by the National Natural Science Foundation of China (Project 21931001, 21871121, 21771156), Technological Innovation Development of Gansu Province (2019ZX-04), Natural Science Foundation of Anhui Province (1908085MB44), Natural Science Foundation of Higher Education Institutions in Anhui province (KJ2019A0524), and the Early Career Scheme (ECS) fund (Grant No.: PolyU 253026/16P) from the Research Grant Council (RGC) in Hong Kong.

Notes and references

1. Y.-S. Wei, M. Zhang, M. Kitta, Z. Liu, S. Horike and Q. Xu, *J. Am. Chem. Soc.,* 2019, **141**, 7906-7916.
2. T. He, X. Xu, B. Ni, H. Lin, C. Li, W. Hu and X. Wang, *Angew. Chem. Int. Ed.,* 2018, **57**, 10148-10152.
3. L. J. De Cock, S. De Koker, B. G. De Geest, J. Grooten, C. Vervaet, J. P. Remon, G. B. Sukhorukov and M. N. Antipina, *Angew. Chem. Int. Ed.,* 2010, **49**, 6954-6973.
4. H. Ke, J. Wang, Z. Dai, Y. Jin, E. Qu, Z. Xing, C. Guo, X. Yue and J. Liu, *Angew. Chem. Int. Ed.,* 2011, **50**, 3017-3021.
5. T. Bollhorst, K. Rezwan and M. Maas, *Chem. Soc. Rev.,* 2017, **46**, 2091-2126.
6. W. Tong, X. Song and C. Gao, *Chem. Soc. Rev.,* 2012, **41**, 6103-6124.
7. J. Zhang, R. J. Coulston, S. T. Jones, J. Geng, O. A. Scherman and C. Abell, *Science,* 2012, **335**, 690-694.
8. S. Cantrill, *Nat. Chem.,* 2012, **4**, 242-242.
9. J. Liu, Y. Lan, Z. Yu, C. S. Y. Tan, R. M. Parker, C. Abell and O. A. Scherman, *Acc. Chem. Res.,* 2017, **50**, 208-217.
10. H. Yin and Z. Tang, *Chem. Soc. Rev.,* 2016, **45**, 4873-4891.
11. G. Fan, F. Li, D. G. Evans and X. Duan, *Chem. Soc. Rev.,* 2014, **43**, 7040-7066.
12. D. Zhou, S. Wang, Y. Jia, X. Xiong, H. Yang, S. Liu, J. Tang, J. Zhang, D. Liu, L. Zheng, Y. Kuang, X. Sun and B. Liu, *Angew. Chem. Int. Ed.,* **2019**, *58*, 736-740.
13. K. He, T. Tadesse Tsega, X. Liu, J. Zai, X.-H. Li, X. Liu, W. Li, N. Ali and X. Qian, *Angew. Chem. Int. Ed.,* 2019, **58**, 11903-11909.
14. L. Trotochaud, S. L. Young, J. K. Ranney and S. W. Boettcher, *J. Am. Chem. Soc.,* **2014, 136**, 6744-6753.
15. X. Long, G. Li, Z. Wang, H. Zhu, T. Zhang, S. Xiao, W. Guo and S. Yang, *J. Am. Chem. Soc*., 2015, **137**, 11900-11903.
16. T.-Y. Wang, G. Nam, Y. Jin, X.-Y. Wang, P.-J. Ren, M.-G. Kim, J.-S. Liang, X.-D. Wen, H. Jang, J.-T. Han, Y.-H. Huang, Q. Li, and J. Cho, *Adv. Mater.,* 2018, **30**, 1800757.
17. J. Ping, Y. Wang, Q. Lu, B. Chen, J. Chen, Y. Huang, Q. Ma, C. Tan, J. Yang, X. Cao, Z. Wang, J. Wu, Y. Ying and H. Zhang, *Adv. Mater.,* **2016**, **28**, 7640-7645.
18 J. Zhang, H. Hu, Z. Li and X. W. Lou, *Angew. Chem. Int. Ed.,* 2016, **55**, 3982-3986.
19. K. Fan, Y. Ji, H. Zou, J. Zhang, B. Zhu, H. Chen, Q. Daniel, Y. Luo, J. Yu and L. Sun, *Angew. Chem. Int. Ed.,* 2017, **56**, 3289-3293.
20. J. Zhang, Z. Li, Y. Chen, S. Gao and X. W. Lou, *Angew. Chem. Int. Ed.,* 2018, **57**, 10944-10948.
21. L. Yu, J.-F. Yang, B.-Y. Guan, Y. Lu and X. W. Lou, *Angew. Chem. Int. Ed.,* 2018, **57**, 172-176.
22. M. Gao, W. Sheng, Z. Zhuang, Q. Fang, S. Gu, J. Jiang and Y. Yan, *J. Am. Chem. Soc*., 2014, **136**, 7077-7084.
23. J. Zhou, H. Li, H. Zhang, H. Li, W. Shi and P. Cheng, *Adv. Mater.,* 2015, **27**, 7072-7077.
24. B. S. Soller, S. Salzinger and B. Rieger, *Chem. Rev.,* 2016, **116**, 1993-2022.
25. J. Ke, J.-W. Xiao, W. Zhu, H. Liu, R. Si, Y.-W. Zhang and C.-H. Yan, *J. Am. Chem. Soc*., 2013, **135**, 15191-15200.
26. Y. Wang, L. Feng, W. Fan, K.-Y. Wang, X. Wang, X. Wang, K. Zhang, X. Zhang, F. Dai, D. Sun and H.-C. Zhou, *J. Am. Chem. Soc*., 2019, **141**, 6967-6975.
27. D. Alezi, A. M. P. Peedikakkal, Ł. J. Weseliński, V. Guillerm, Y. Belmabkhout, A. J. Cairns, Z. Chen, Ł. Wojtas and M. Eddaoudi, *J. Am. Chem. Soc*., 2015, **137**, 5421-5430.

28. Y. Liu, M. Pan, Q.-Y. Yang, L. Fu, K. Li, S.-C. Wei and C.-Y. Su, *Chem. Mater.,* 2012, **24**, 1954-1960.
29. D. F. Sava, L. E. S. Rohwer, M. A. Rodriguez and T. M. Nenoff, *J. Am. Chem. Soc*., 2012, **134**, 3983-3986.
30. X. Rao, T. Song, J. Gao, Y. Cui, Y. Yang, C. Wu, B. Chen and G. Qian, *J. Am. Chem. Soc*., 2013, **135**, 15559-15564.
31. S.-Y. Zhang, W. Shi, P. Cheng and M. J. Zaworotko, *J. Am. Chem. Soc*., 2015, **137**, 12203-12206.
32. V. Guillerm, Ł. J. Weseliński, Y. Belmabkhout, A. J. Cairns, V. D'Elia, Ł. Wojtas, K. Adil and M. Eddaoudi, *Nat. Chem.,* 2014, **6**, 673-680.
33. L. Zhang, S. Yuan, L. Feng, B. Guo, J.-S. Qin, B. Xu, C. Lollar, D. Sun and H.-C. Zhou, *Angew. Chem. Int. Ed.,* 2018, **57**, 5095-5099.
34. N. Li, J. Xu, R. Feng, T.-L. Hu and X.-H. Bu, *Chem. Commun.,* 2016, *52*, 8501-8513.
35. M. Y. Masoomi, A. Morsali, A. Dhakshinamoorthy and H. Garcia, *Angew. Chem. Int. Ed.,* 2019, **58**, 15188-15205.
36. M. A. Syzgantseva, C. P. Ireland, F. M. Ebrahim, B. Smit and O. A. Syzgantseva, *J. Am. Chem. Soc*., 2019, **141**, 6271-6278.
37. P. Falcaro and S. Furukawa, *Angew. Chem. Int. Ed.,* 2012, **51**, 8431-8433.
38. G. Skorupskii, B. A. Trump, T. W. Kasel, C. M. Brown, C. H. Hendon and M. Dincă, *Nat. Chem*., 2020, **12**, 131-136.
39. K. Wu, L.-D. Sun and C.-H. Yan, *Adv. Energy Mater.,* 2016, **6**, 1600501.
40. J. A. Rodriguez, D. C. Grinter, Z. Liu, R. M. Palomino and S. D. Senanayake, *Chem. Soc. Rev.,* 2017, **46**, 1824-1841.
41. Y. Xiang, X.-F. Yu, D.-F. He, Z. Sun, Z. Cao and Q.-Q. Wang, *Adv. Funct. Mater.,* 2011, **21**, 4388-4396.
42. X.-P. Wu, L. Gagliardi and D. G. Truhlar, *J. Am. Chem. Soc.,* 2018, **140**, 7904-7912.
43. A. Chen, X. Yu, Y. Zhou, S. Miao, Y. Li, S. Kuld, J. Sehested, J. Liu, T. Aoki, S. Hong, M. F. Camellone, S. Fabris, J. Ning, C. Jin, C. Yang, A. Nefedov, C. Wöll, Y. Wang and W. Shen, *Nat. Catal*. 2019, **2**, 334-341.
44. J.-S. Yao, J. Ge, B.-N. Han, K.-H. Wang, H.-B. Yao, H.-L. Yu, J.-H. Li, B.-S. Zhu, J.-Z. Song, C. Chen, Q. Zhang, H.-B. Zeng, Y. Luo and S.-H. Yu, *J. Am. Chem. Soc*., 2018, **140**, 3626-3634.
45. K. Fan, H. Chen, Y. Ji, H. Huang, P. M. Claesson, Q. Daniel, B. Philippe, H. Rensmo, F. Li, Y. Luo and L. Sun, *Nat. Commun*., 2016, **7**, 11981.
46. Q. Wang, L. Shang, R. Shi, X. Zhang, Y. Zhao, G. I. N. Waterhouse, L.-Z. Wu, C.-H. Tung and T. Zhang, *Adv. Energy Mater*., 2017, **7**, 1700467.
47. H.-J. Xu, B.-K. Wang, C.-P. Shan, P.-X. Xi, W.-S. Liu and Y. Tang, *ACS Appl. Mater. Interfaces,* 2018, **10**, 6336-6345.
48. J. Bao, X. Zhang, B. Fan, J. Zhang, M. Zhou, W. Yang, X. Hu, H. Wang, B. Pan and Y. Xie, *Angew. Chem. Int. Ed.*, 2015, **54**, 7399-7404.
49. J. Yin, Y. Li, F. Lv, M. Lu, K. Sun, W. Wang, L. Wang, F. Cheng, Y. Li, P. Xi and S. Guo, *Adv. Mater.*, 2017, **29**, 1704681.
50. H. Xu, J. Cao, C. Shan, B. Wang, P. Xi, W. Liu, and Y. Tang, *Angew. Chem. Int. Ed*., 2018, **57**, 8654-8658.
51. D. Friebel, M. W. Louie, M. Bajdich, K. E. Sanwald, Y. Cai, A. M. Wise, M.-J. Cheng, D. Sokaras, T.-C. Weng, R. Alonso-Mori, R. C. Davis, J. R. Bargar, J. K. Nørskov, A. Nilsson and A. T. Bell, *J. Am. Chem. Soc*., 2015, **137**, 1305-1313.
52. J. Y. C. Chen, L. Dang, H. Liang, W. Bi, J. B. Gerken, S. Jin, E. E. Alp and S. S. Stahl, *J. Am. Chem. Soc*., 2015, **137**, 15090-15093.
53. Z. Cai, D.-J. Zhou, M.-Y. Wang, S. M. Bak, Y.-S. Wu, Z.-S. Wu, Y. Tian, X.-Y. Xiong, Y.-P. Li, W. Liu, S. Siahrostami, Y. Kuang, X.-Q. Yang, H.-H. Duan, Z.-X. Feng, H.-L. Wang and X.-M. Sun, *Angew. Chem. Int. Ed.,* 2018, **57**, 9392-9396.
54. C. T. Palumbo, I. Zivkovic, R. Scopelliti and M. Mazzanti, *J. Am. Chem. Soc.,* 2019, **141**, 9827-9831.
55. N. T. Rice, I. A. Popov, D. R. Russo, J. Bacsa, E. R. Batista, P. Yang, J. Telser and H. S. La Pierre, *J. Am. Chem. Soc*., 2019, **141**, 13222-13233.
56. B.Huang, *J. Comput. Chem*, 2016, **37**, 825-835.

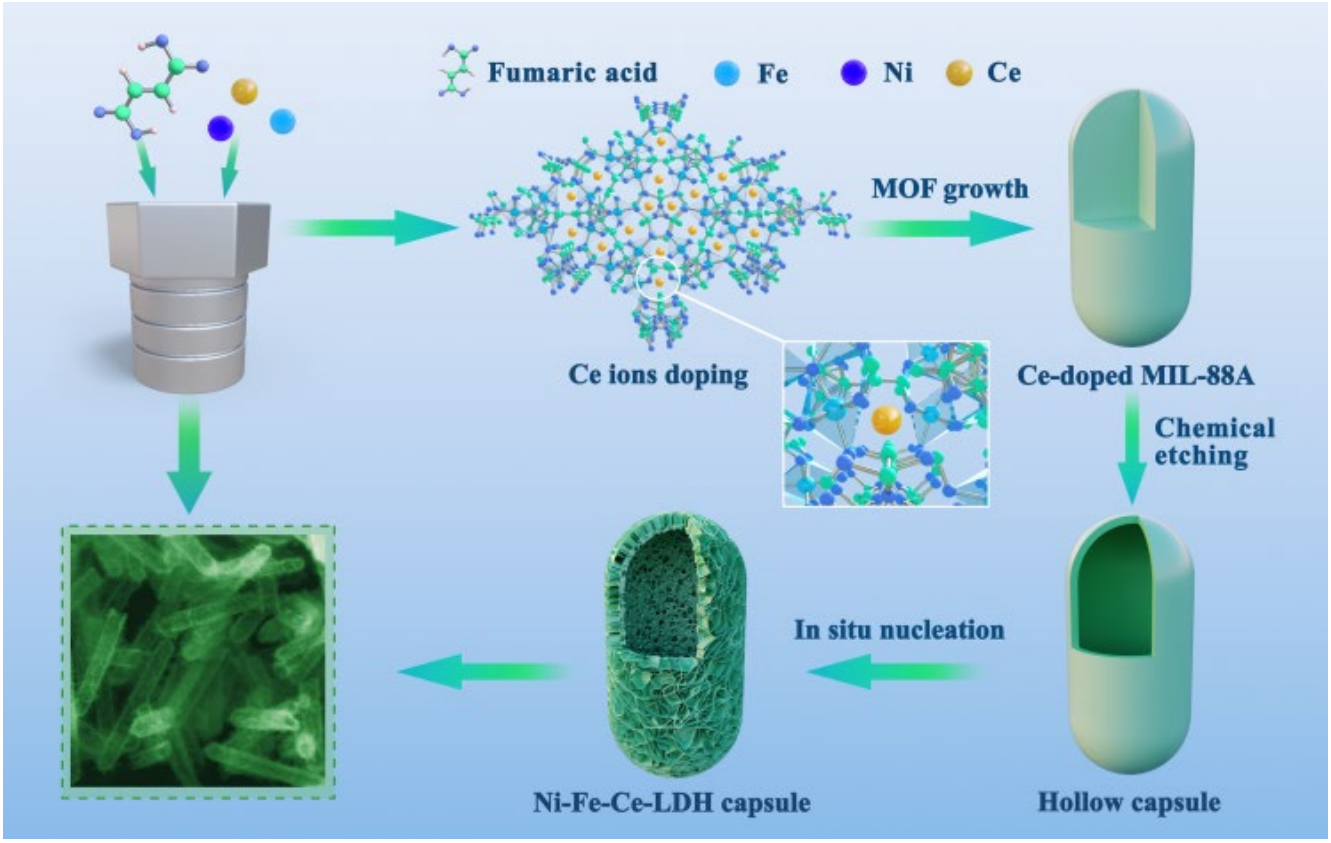

Fig. 2 Schematic illustration of the fabrication of hollow Ni-Fe-Ce-LDH microcapsules mediated by cerium doping MIL-88A.

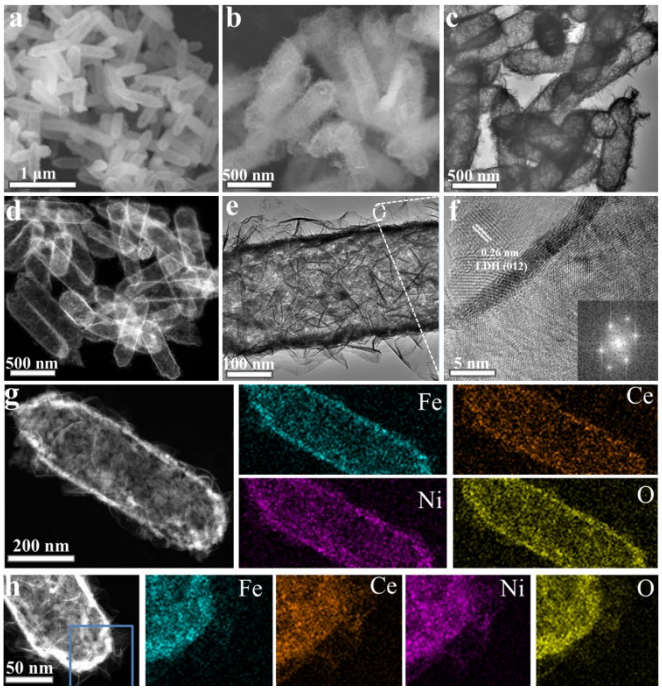

Fig. 1 (a,b) SEM and (c) TEM images of the 30%Ce-NiFe-LDH microcapsules. (d) HAADF-STEM image and (e,f) HRTEM images and corresponding SAED pattern (the inset) of the 30%Ce-Ni-Fe-LDH. (g,h) A single microcapsule and local magnified microcapsule for HAADF-STEM image and elemental mapping images of 30%Ce-NiFe-LDH microcapsules.

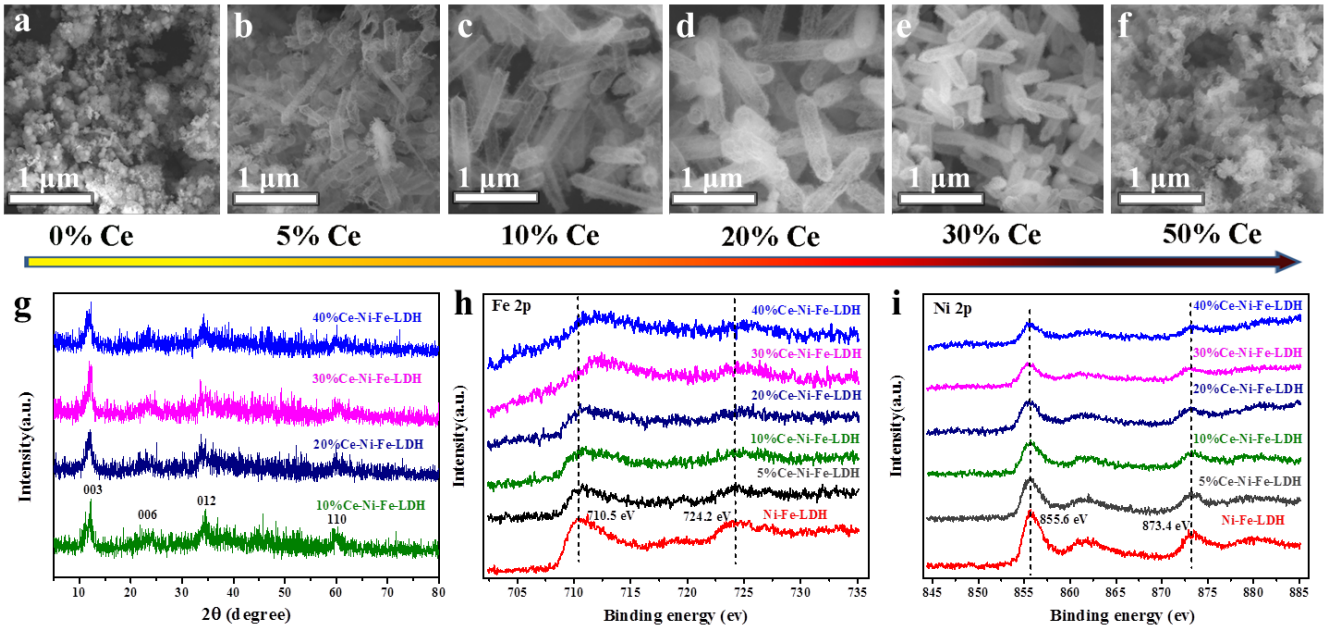

Fig. 4 SEM images of Ni-Fe-Ce-LDH obtained by adding different volumes of Ce ions into the synthetic solution. (a) Fe/Ce = 1:0, (b) Fe/Ce = 0.95:0.05, (c) Fe/Ce = 0.9:0.1, (d) Fe/Ce = 0.8:0.2, (e) Fe/Ce = 0.7:0.3, (f) Fe/Ce = 0.5:0.5. (g) XRD patterns of Ni-Fe-Ce-LDH. Comparison of XPS spectra and electrochemical performance of Ni-Fe-LDH and Ni-Fe-Ce-LDH. (h) Fe-2p and (i) Ni-2p XPS spectra of Ni-Fe-LDH and Ni-Fe-Ce-LDH.

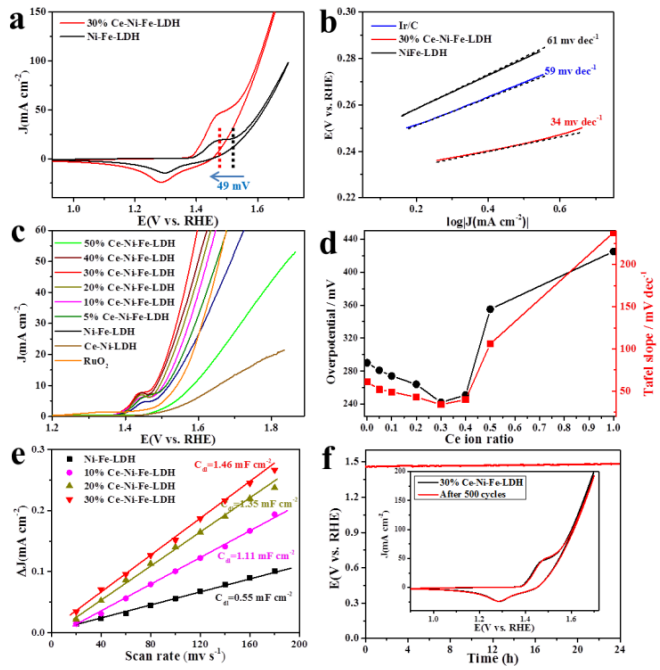

Fig. 3 Comparison of electrochemical performance of Ni-Fe-LDH and Ni-Fe-Ce-LDH. (a) cyclic voltammetry curves of Ni-Fe-LDH and 30%Ce-Ni-Fe-LDH. (b) The Tafel slopes of the Ir/C, Ni-Fe-LDH and 30% Ce-Ni-Fe-LDH. (c) Polarization curves of Ni-Fe-Ce-LDH with different Ce/Fe ratio. (d) The OER overpotential (black line) at 10 mA cm^{-2} and Tafel slopes (red line) for different Ce doping ratio. (e) Capacitive J versus scan rate for Ni-Fe-LDH and Ni-Fe-Ce-LDH. (f) Chronopotentiometric curve of water electrolysis for Ni-Fe-LDH and 30%Ce-Ni-Fe-LDH. The inset in (f) shows the CV curves for 30%Ce-Ni-Fe-LDH (black) and after 500 (red) CV sweeps.

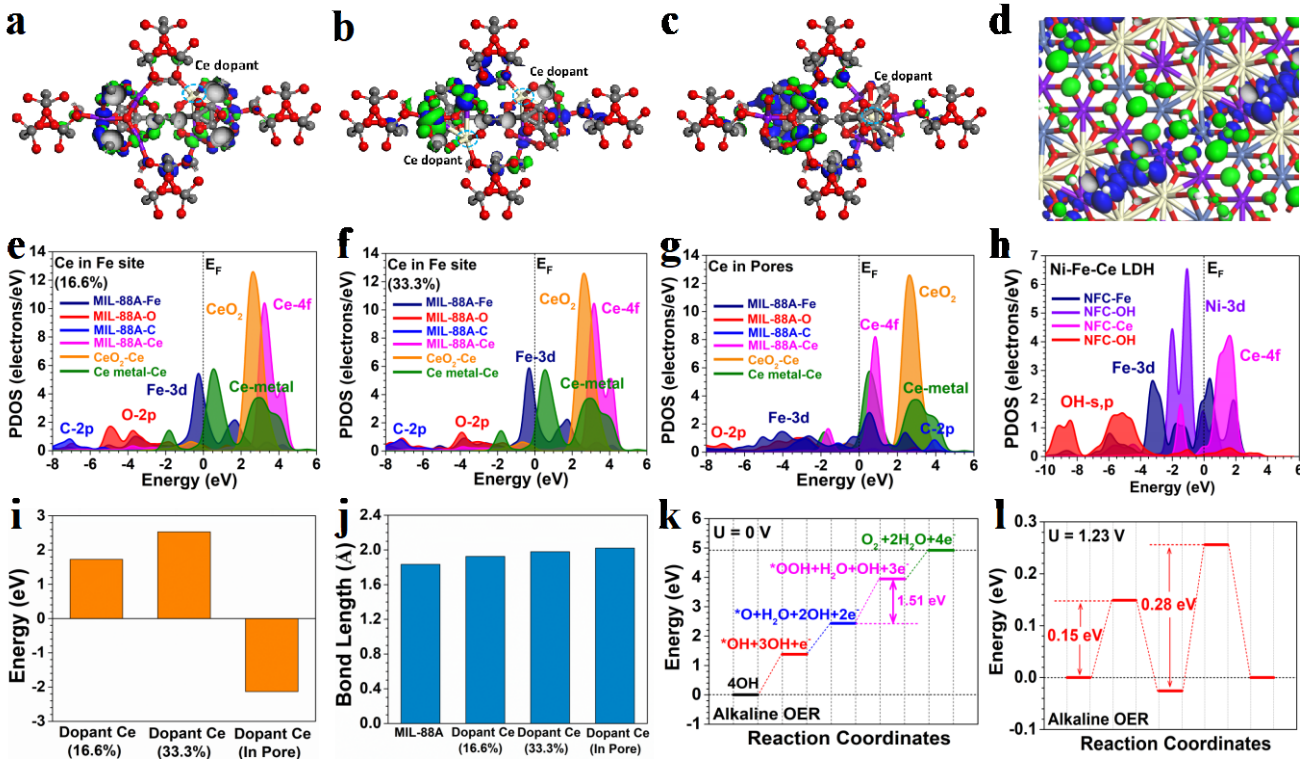

Fig. 5 The theoretical calculations of Ce doping in MIL-88A and the OER performances of Ni-Fe-Ce LDH. (a) The top view of the real spatial 3D orbital contour plots with Ce doping concentration of 16.6% in Fe sites. (b) The top view of the real spatial 3D orbital contour plots with Ce doping concentration of 33.3% in Fe sites. (c) The top view of the real spatial 3D orbital contour plots with Ce doping in the pores of MIL-88A. Ce dopants in the MIL-88A are indicated by the blue circle. (d) The top view of the real spatial 3D orbital contour plots in Ni-Fe-Ce-LDH. Purple balls = Fe; Beige balls = Ce; Blue balls = Ni; Red ball = O; Grey balls = C; White balls = H. (e) The PDOS of Ce-doped MIL-88A of 16.6% concentration. (f) The PDOS of Ce-doped MIL-88A of 33.3 % concentration. (g) The PDOS of Ce dopants in the pores within MIL-88A. (h) The PDOS of Ni-Fe-Ce-LDH. (i) The formation energies of Ce doping at different positions and concentrations. (j) The bond length change of Fe-O in MIL-88A with different doping positions and concentrations. (k) The energy diagram of the OER performance by Ni-Fe-Ce-LDH under U = 0 V. (l) The alkaline OER pathway at U = 1.23 V.